

PANEL-PIN MODEL FOR KINEMATIC AND EQUILIBRIUM ANALYSIS OF RIGID ORIGAMI

Kentaro HAYAKAWA¹ and Makoto OHSAKI¹

¹Dr. Eng., Dept. of Architecture and Architectural Engineering, Kyoto University, Kyoto-Daigaku Katsura, Nishikyo, Kyoto 615-8540, Japan, se.hayakawa@archi.kyoto-u.ac.jp, ohsaki@archi.kyoto-u.ac.jp

Editor's Note: The first author of this paper is one of the four winners of the 2023 Hangai Prize, awarded for outstanding papers that are submitted for presentation and publication at the annual IASS Symposium by younger members of the Association (under 30 years old). It is published here with permission of the editors of the proceedings of the IASS Symposium 2023 "Integration of Design and Fabrication", that was held in July 2023, in Melbourne, Australia.

DOI: <https://doi.org/10.20898/j.iass.2023.025>

ABSTRACT

In this study, the mathematical model referred to as the panel-pin model is proposed for analyzing the infinitesimal-deformation mechanism and the large-deformation equilibrium path of a rigid origami composed of rigid faces (panels) and subjected to deformation only at its crease lines. The panel-pin model represents a rigid origami as a structure of rigid panels pin-connected at the vertices and has the following advantages: 1) consistent formulation of compatibility equations for any type of the rigid origami structure; 2) systematic computation of vertex displacements, folding angles, and their derivatives; and 3) ease of accounting for gravity acting on the panels. The infinitesimal mechanism of the panel-pin model is studied according to the standard procedure for mechanisms and linkages, and an equilibrium path is traced as the trajectory of equilibrium points obtained by minimizing the total potential energy of the model with a rotational spring along each crease line. The numerical examples with multiple degrees of freedom of the mechanism show that the multiple equilibrium paths can be obtained by assigning the initial imperfection, and this is also confirmed by the physical model.

Keywords: rigid origami, kinematics, equilibrium, energy minimization, geometrically nonlinear analysis

1. INTRODUCTION

Rigid origami is folded and unfolded within strict constraints, with its faces remaining undeformed during the folding process. It has wide range of potential engineering applications; e.g., solar panels on artificial satellites [1], robots [2], and transformable building envelopes [3]. Consequently, the analysis and simulation of folding properties are crucial to effectively exploit the deformation mechanisms of rigid origami, and numerous models and methods have been proposed in this respect [4].

The rotation hinge model [5, 6] in Fig. 1(a) and the truss model [7, 8] in Fig. 1(b) are commonly used for kinematic analysis of rigid origami. In the former model, folding angles are treated as independent variables, and a folding state can be expressed with fewer variables than other models. However, its complicated expression of vertex positions makes it difficult to incorporate displacement boundary conditions and external loads applied to vertices.

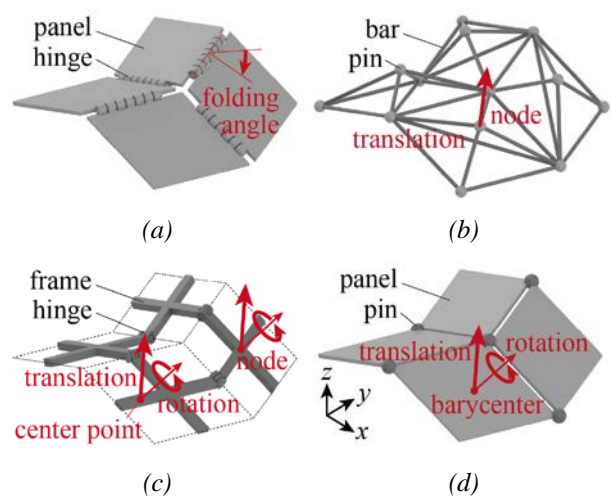


Figure 1: Models representing the deformation mechanism of rigid origami whose variables are indicated by red.
(a) Rotation hinge model, (b) Truss model, (c) Frame model, (d) Panel-pin model

In contrast, the latter model consists of rigid bars placed along the edges and treats the nodal

translations as variables, making it easy to fix nodal displacements and to apply nodal loads. The disadvantage of this model is its complicated configuration for modelling a face with more than three edges; diagonal members must be arranged for ensuring the in-plane rigidity, and trigonometric geometric constraints [7] or the three-dimensional member assemblages [8] are necessary for ensuring the out-of-plane rigidity. The frame model in Fig. 1(c) has also been developed [9, 10], which consists of frame members hinge-connected at each crease line and rigidly connected at the node on each face. Although a folding path tracing method of this model has been proposed [10], this is not suitable for large models due to the high computational cost associated with a large number of variables.

In this study, a panel-pin model shown in Fig. 1(d) is proposed for providing a simpler manner of ensuring the rigidity of faces compared to the truss model, while requiring fewer variables than the frame model. The proposed model is highly versatile and can be applied to a wide range of analyses considering gravity, point loads, forced displacements, and support conditions. This model offers following advantages;

- 1) Consistent formulation of compatibility equations for describing the deformation mechanism of the model including holes or faces with more than three sides,
- 2) Systematic computation of vertex displacements, folding angles, and their derivatives, and
- 3) Ease of accounting for gravity acting on the panels.

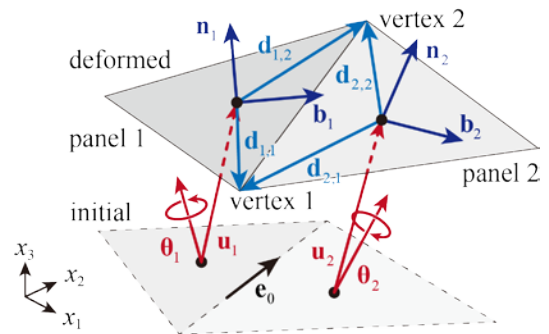
The panel-pin model employs translation and rotation of the centers of gravity of rigid panels as independent variables, which are often used in the classical models of linkages. However, the formulation of the compatibility equations over these variables is different from that for linkages; the panels are pin-connected at the vertices instead of being joined by hinges. The vertex displacements and folding angles are treated as nonlinear functions of the panel displacements. The displacement boundary conditions on the vertices are incorporated as additional compatibility equations. The infinitesimal mechanism of the panel-pin model is determined from the derivatives of the compatibility equations. An equilibrium state under loads is determined by minimizing the total potential energy under the compatibility constraints after adding

rotational springs along the crease lines. An equilibrium path is traced by sequentially updating the forced displacements, as proposed in Ref. [10].

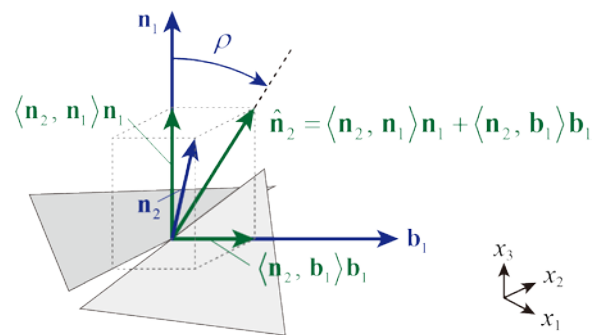
2. PANEL-PIN MODEL

2.1. Compatibility Equations and Folding Angle at a Single Crease Line

Suppose vertices 1 and 2 are the endpoints of the crease line, and denote a unit vector directed from vertices 1 to 2 at the initial state by $\mathbf{e}^0 \in \mathbb{R}^3$. Note that the superscript 0 indicates the value of the vector at the initial state. In addition, let \mathbf{n}_i and $\mathbf{d}_{i,j}^0 \in \mathbb{R}^3$ denote the unit normal vector of panel i and the vector from the barycenter of panel i to vertex j ($i, j = 1, 2$), respectively, at the initial state. The directions of the unit panel normal vectors are determined in the same side of the origami, and the local panel indices are determined so that panels 1 and 2 satisfies $\langle \mathbf{n}_1^0, \mathbf{d}_{1,1}^0 \times \mathbf{d}_{1,2}^0 \rangle > 0$ and $\langle \mathbf{n}_2^0, \mathbf{d}_{2,1}^0 \times \mathbf{d}_{2,2}^0 \rangle < 0$, respectively, where $\langle \cdot, \cdot \rangle$ stands for the inner product of two vectors. $\mathbf{b}_i^0 \in \mathbb{R}^3$ ($i = 1, 2$) is also defined such that $\mathbf{b}_i^0 = \mathbf{e}^0 \times \mathbf{n}_i^0$. Note that at the initial state, the crease lines may have non-zero folding angles.



(a)



(b)

Figure 2: Definitions of vectors. (a) Reference vectors of panels, (b) Vectors for calculating the folding angle

Let \mathbf{u}_i and $\boldsymbol{\theta}_i \in \mathbb{R}^3$ denote the translation and rotation vectors of panel i , respectively, in the global coordinate system (x_1, x_2, x_3) . As shown in Fig. 2(a), \mathbf{n}_i , $\mathbf{d}_{i,j}$, and $\mathbf{b}_i \in \mathbb{R}^3$ ($i, j = 1, 2$) are defined as

$$\begin{aligned} \mathbf{n}_i &= \mathbf{R}(\boldsymbol{\theta}_i)\mathbf{n}_i^0 \\ \mathbf{d}_{i,j} &= \mathbf{R}(\boldsymbol{\theta}_i)\mathbf{d}_{i,j}^0 \\ \mathbf{b}_i &= \mathbf{R}(\boldsymbol{\theta}_i)\mathbf{b}_i^0 \end{aligned} \quad (1)$$

where $\mathbf{R}(\boldsymbol{\theta}_i) \in \mathbb{R}^{3 \times 3}$ is the Rodrigues' rotation matrix [11] with respect to $\boldsymbol{\theta}_i$. Using these vectors, the translation vector $\mathbf{v}_j^i \in \mathbb{R}^3$ ($i, j = 1, 2$) of vertex j can be evaluated from both panels 1 and 2 as

$$\mathbf{v}_j^i = \mathbf{u}_i + \mathbf{d}_{i,j} - \mathbf{d}_{i,j}^0 = \mathbf{u}_i + (\mathbf{R}(\boldsymbol{\theta}_i) - \mathbf{I}_3)\mathbf{d}_{i,j}^0 \quad (i = 1, 2) \quad (2)$$

where $\mathbf{I}_3 \in \mathbb{R}^{3 \times 3}$ is the identity matrix. Since $\mathbf{v}_j^1 = \mathbf{v}_j^2$ should be satisfied, the compatibility equation for the displacements of panels 1 and 2 at vertex j ($= 1, 2$) is formulated as follows:

$$\begin{aligned} \Delta \mathbf{u}_j^{1,2} &= \mathbf{u}_1 + (\mathbf{R}(\boldsymbol{\theta}_1) - \mathbf{I}_3)\mathbf{d}_{1,j}^0 \\ &\quad - \mathbf{u}_2 - (\mathbf{R}(\boldsymbol{\theta}_2) - \mathbf{I}_3)\mathbf{d}_{2,j}^0 = \mathbf{0} \end{aligned} \quad (3)$$

Furthermore, folding angle ρ ($-\pi < \rho \leq \pi$) of the crease line between panels 1 and 2 is defined as

$$\rho = \text{atan2}(\langle \mathbf{n}_2, \mathbf{b}_1 \rangle, \langle \mathbf{n}_2, \mathbf{n}_1 \rangle) \quad (4)$$

where $\text{atan2}(y, x)$ is the 2-argument arctangent available in various programming languages. As shown in Fig. 2(b), ρ defined in Eq. (4) is the angle between \mathbf{n}_1 and $\hat{\mathbf{n}}_2 = \langle \mathbf{n}_2, \mathbf{n}_1 \rangle \mathbf{n}_1 + \langle \mathbf{n}_2, \mathbf{b}_1 \rangle \mathbf{b}_1$, which is a vector obtained by projecting \mathbf{n}_2 onto the plane spanned by \mathbf{n}_1 and \mathbf{b}_1 . When $\Delta \mathbf{u}_1^{1,2} = \Delta \mathbf{u}_2^{1,2} = \mathbf{0}$ is satisfied, $\mathbf{n}_2 = \hat{\mathbf{n}}_2$, $\sin \rho = \langle \mathbf{n}_2, \mathbf{b}_1 \rangle$, and $\cos \rho = \langle \mathbf{n}_2, \mathbf{n}_1 \rangle$ hold. According to Eq. (1), ρ is the function of only $\boldsymbol{\theta}_1$ and $\boldsymbol{\theta}_2$, and its derivatives can be systematically calculated using the derivatives of the rotation matrices.

Remark 1 By using $\text{atan2}(y, x)$ function instead of arcsin or arccos function, ρ and its partial derivatives can be compatibly calculated even when $\Delta \mathbf{u}_1^{1,2} \neq \mathbf{0}$ or $\Delta \mathbf{u}_2^{1,2} \neq \mathbf{0}$.

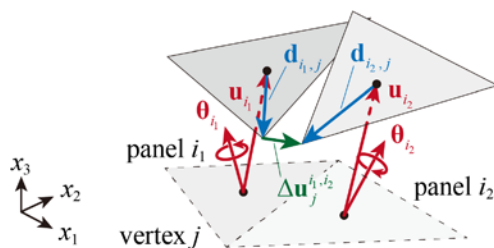


Figure 3: Incompatibility of the displacements of panels i_1 and i_2 at vertex j

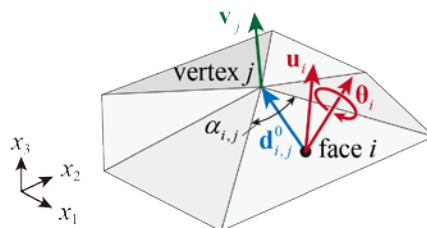


Figure 4: Translational displacement of vertex j

2.2. Compatibility Equations for Entire Rigid Origami and Displacements of Vertices

Let N^c , N^p , and N^v denote the number of crease lines, panels (faces), and vertices of a rigid origami, respectively. The *generalized displacement vector* $\mathbf{X} \in \mathbb{R}^N$ is defined as the assemblage of the components of \mathbf{u}_i and $\boldsymbol{\theta}_i$ for all $i = 1, \dots, N^p$ where $N = 6N^p$. When adjacent panels i_1 and i_2 ($= 1, \dots, N^p$) are connected at vertex j ($= 1, \dots, N^v$) as shown in Fig. 3, the compatibility equation for the displacements of panels i_1 and i_2 at vertex j is formulated from Eq. (3) as

$$\begin{aligned} \Delta \mathbf{u}_j^{i_1,i_2}(\mathbf{X}) &= \mathbf{u}_{i_1} + (\mathbf{R}(\boldsymbol{\theta}_{i_1}) - \mathbf{I}_3)\mathbf{d}_{i_1,j}^0 \\ &\quad - \mathbf{u}_{i_2} - (\mathbf{R}(\boldsymbol{\theta}_{i_2}) - \mathbf{I}_3)\mathbf{d}_{i_2,j}^0 = \mathbf{0} \end{aligned} \quad (5)$$

Its physical interpretation is illustrated in Fig. 3. Since Eq. (5) is formulated at every endpoint of the crease line, there are in total $6N^c$ compatibility conditions for the entire rigid origami. Here, all $\Delta \mathbf{u}_j^{i_1,i_2}(\mathbf{X})$ are assembled into a vector $\Delta \mathbf{U}(\mathbf{X}) \in \mathbb{R}^{6N^c}$, and the compatibility equation for the entire rigid origami is formulated as $\Delta \mathbf{U}(\mathbf{X}) = \mathbf{0}$.

Next, we reformulate the translation of a vertex. Although it can be written as in Eq. (2), the different formulation is used to include the case where $\Delta \mathbf{U}(\mathbf{X}) \neq \mathbf{0}$. Let \mathcal{I}_j denote the set of indices of panels around vertex j ($= 1, \dots, N^v$), and $\alpha_{i,j}$

($i \in \mathcal{I}_j$) denote the inner angle of panel i at vertex j as shown in Fig. 4. The translation vector $\mathbf{v}_j(\mathbf{X}) \in \mathbb{R}^3$ ($j=1, \dots, N^v$) of vertex j is calculated as follows:

$$\mathbf{v}_j(\mathbf{X}) = \frac{1}{A_j} \sum_{i \in \mathcal{I}_j} \alpha_{i,j} \{ \mathbf{u}_i + (\mathbf{R}(\boldsymbol{\theta}_i) - \mathbf{I}_3) \mathbf{d}_{i,j}^0 \} \quad (6)$$

$$A_j = \sum_{i \in \mathcal{I}_j} \alpha_{i,j}$$

Remark 2 $\mathbf{v}_j(\mathbf{X})$ defined in Eq. (6) is the weighted average of the positions of panel vertices around vertex j , and reasonably estimates the position of vertex j when $\Delta \mathbf{U}(\mathbf{X}) \neq \mathbf{0}$. \mathbf{v}_j and its partial derivatives with respect to the panel displacements can be compatibly calculated even when $\Delta \mathbf{U}(\mathbf{X}) \neq \mathbf{0}$.

Suppose the displacement of vertex j ($=1, \dots, N^v$) in the x_k -direction ($k=1, 2, 3$) denoted by $v_j^{(k)}(\mathbf{X})$ is fixed, and let \mathcal{J}^f denote the set of index pairs of the vertices and the fixed directions. When the number of components of \mathcal{J}^f is N^f , $v_j^{(k)}(\mathbf{X})$ for all $\{j, k\} \in \mathcal{J}^f$ are assembled into a vector $\Delta \mathbf{V}^f(\mathbf{X}) \in \mathbb{R}^{N^f}$. In addition, we also consider the forced vertex displacements, and let \mathcal{J}^d represent the set of index pairs of the vertices and the directions to which the forced displacements are applied. The non-zero target value of $v_j^{(k)}(\mathbf{X})$ ($\{j, k\} \in \mathcal{J}^d$; $j=1, \dots, N^v$; $k=1, 2, 3$) is denoted by $v_j^{d(k)}$, and $v_j^{(k)}(\mathbf{X}) - v_j^{d(k)}$ for all $\{j, k\} \in \mathcal{J}^d$ are assembled into a vector $\Delta \mathbf{V}^d(\mathbf{X}) \in \mathbb{R}^{N^d}$ where N^d is the number of components of \mathcal{J}^d . Here, $\Delta \mathbf{U}(\mathbf{X})$, $\Delta \mathbf{V}^f(\mathbf{X})$, and $\Delta \mathbf{V}^d(\mathbf{X})$ are combined into a column vector $\mathbf{C}(\mathbf{X}) = (\Delta \mathbf{U}(\mathbf{X})^T, \Delta \mathbf{V}^f(\mathbf{X})^T, \Delta \mathbf{V}^d(\mathbf{X})^T)^T \in \mathbb{R}^M$ which is referred to as the *incompatibility vector*. The number of components of $\mathbf{C}(\mathbf{X})$ is calculated as $M = 6N^c + N^f + N^d$. Then, the compatibility equations representing the panel connectivity, fixed vertex displacements, and the forced vertex displacements are collectively written in a vector form as

$$\mathbf{C}(\mathbf{X}) = \mathbf{0} \quad (7)$$

3. INFINITESIMAL MECHANISM ANALYSIS

3.1. First-order Infinitesimal Mechanism

An infinitesimal mechanism of a panel-pin model is investigated to comprehend the degrees of freedom of the mechanism and the deformation modes in the range of infinitesimal deformation. It is evaluated in the same manner as the basic procedure for other models [4–9]. To compatibly incorporate the degrees of freedom corresponding to the forced displacements, $\Delta \mathbf{V}^d(\mathbf{X}) = \mathbf{0}$ is replaced to constrain the relative displacements among the vertices where the forced displacements are assigned. When $N^d = 1$, the constraint for the forced displacement is not necessary. When $N^d > 1$, a single pair $\{\bar{j}, \bar{k}\}$ is selected from \mathcal{J}^d , and the constraint between $v_j^{(k)}(\mathbf{X})$ and $v_{\bar{j}}^{(\bar{k})}(\mathbf{X})$ is formulated as

$$\frac{1}{v_j^{d(k)}} v_j^{(k)}(\mathbf{X}) - \frac{1}{v_{\bar{j}}^{d(\bar{k})}} v_{\bar{j}}^{(\bar{k})}(\mathbf{X}) = 0 \quad (8)$$

$$(\{j, k\}, \{\bar{j}, \bar{k}\} \in \mathcal{J}^d; \{j, k\} \neq \{\bar{j}, \bar{k}\})$$

There are $N^d - 1$ constraints on the relative vertex displacements, and the left-hand sides of Eq (8) for all $\{j, k\} \in \mathcal{J}^d \setminus \{\bar{j}, \bar{k}\}$ are assembled into a vector $\Delta \bar{\mathbf{V}}^d(\mathbf{X}) \in \mathbb{R}^{N^d - 1}$. In the following, the argument \mathbf{X} will be omitted for simple expression. Defining $\bar{\mathbf{C}} = (\Delta \mathbf{U}^T, \Delta \mathbf{V}^f{}^T, \Delta \bar{\mathbf{V}}^d{}^T)^T \in \mathbb{R}^{M-1}$, the *first-order infinitesimal mechanism* is represented by a vector $\mathbf{X}' \in \mathbb{R}^N$ satisfying [6, 12]

$$\frac{d\bar{\mathbf{C}}}{d\mathbf{X}} \mathbf{X}' = \mathbf{0} \quad (9)$$

$d\bar{\mathbf{C}}/d\mathbf{X} \in \mathbb{R}^{(M-1) \times N}$ is the *compatibility matrix* whose (i, j) component is $\partial \bar{C}_i / \partial X_j$ where the subscript i such as \bar{C}_i represents the i -th component of a vector. \mathbf{X}' satisfying Eq. (9) is in the null-space of $d\bar{\mathbf{C}}/d\mathbf{X}$ whose dimension is $N - \text{rank}(d\bar{\mathbf{C}}/d\mathbf{X})$, which is referred to as the number of kinematic indeterminacy, and its bases are referred to as the *infinitesimal mechanism modes*. Note that if the infinitesimal mechanism is investigated by using $d\mathbf{C}/d\mathbf{X}$ instead of $d\bar{\mathbf{C}}/d\mathbf{X}$, the forced displacements are regarded as the fixed displacement conditions. We can also define a *generalized self-equilibrium force* $\bar{\mathbf{F}} \in \mathbb{R}^{M-1}$ which satisfies [6, 12]

$$\bar{\mathbf{F}}^T \frac{d\bar{\mathbf{C}}}{d\mathbf{X}} = \mathbf{0} \tag{10}$$

The self-equilibrium force $\bar{\mathbf{F}}$ satisfying Eq. (10) is in the left null-space of $d\bar{\mathbf{C}}/d\mathbf{X}$ whose dimension is $M - 1 - \text{rank}(d\bar{\mathbf{C}}/d\mathbf{X})$, which is referred to as the number of statical indeterminacy.

3.2. Second-order Infinitesimal Mechanism

Equations for the *second-order infinitesimal mechanism* are presented below for completeness of the paper. For a first-order infinitesimal mechanism \mathbf{X}' satisfying Eq. (9), the second-order infinitesimal mechanism is represented by a pair of vectors $(\mathbf{X}', \mathbf{X}'') \in (\mathbb{R}^N, \mathbb{R}^N)$ satisfying [6, 12]

$$\frac{d\bar{\mathbf{C}}}{d\mathbf{X}} \mathbf{X}'' + \left[\frac{d^2\bar{\mathbf{C}}}{d\mathbf{X}^2} \mathbf{X}' \right] \mathbf{X}' = \mathbf{0} \tag{11}$$

where $d^2\bar{\mathbf{C}}/d\mathbf{X}^2$ is the $(M - 1) \times N \times N$ order-3 tensor whose (i, j, k) component is $\partial^2\bar{C}_i/\partial X_j \partial X_k$.

The (i, j) component of $[(d^2\bar{\mathbf{C}}/d\mathbf{X}^2)\mathbf{X}'] \in \mathbb{R}^{(M-1) \times N}$ is $\sum_{k=1}^N (\partial^2\bar{C}_i/\partial X_j \partial X_k) X'_k$. The second-order infinitesimal mechanism $(\mathbf{X}', \mathbf{X}'')$ exists if and only if \mathbf{X}' satisfying Eq. (9) satisfies the following equation for any $\bar{\mathbf{F}}$ satisfying Eq. (10) [6, 12]:

$$\bar{\mathbf{F}}^T \left[\frac{d^2\bar{\mathbf{C}}}{d\mathbf{X}^2} \mathbf{X}' \right] \mathbf{X}' = \mathbf{X}'^T \left[\bar{\mathbf{F}}^T \frac{d^2\bar{\mathbf{C}}}{d\mathbf{X}^2} \right] \mathbf{X}' = 0 \tag{12}$$

where the (i, j) component of $[\bar{\mathbf{F}}^T (d^2\bar{\mathbf{C}}/d\mathbf{X}^2)] \in \mathbb{R}^{N \times N}$ is calculated as $\sum_{k=1}^{M-1} \bar{F}_k (\partial^2\bar{C}_k/\partial X_i \partial X_j)$.

4. EQUILIBRIUM PATH ANALYSIS UNDER GRAVITY

4.1. Finding an Equilibrium Point

An equilibrium state of a panel-pin model is obtained by the energy minimization approach [10]. To stabilize and uniquely determine the equilibrium state, rotational stiffness is assigned to each crease line. The moment around crease line k ($= 1, \dots, N^c$) is calculated as $K_k(\rho_k - \rho_k^0)$ for the constant K_k where ρ_k^0 is the initial folding angle of crease line k . Let w_i and $u_i^{\text{ref}(3)}$ denote the weight and the reference height of the barycenter of panel i , respectively, to determine the potential energy of the

gravity in the x_3 -direction. When the constant point load $\mathbf{p}_j \in \mathbb{R}^3$ ($j = 1, \dots, N^v$) is applied to vertex j , the total potential energy of the panel-pin model is defined as the function of \mathbf{X} as

$$\begin{aligned} \Pi(\mathbf{X}) = & \frac{1}{2} \sum_{k=1}^{N^c} K_k (\rho_k(\mathbf{X}) - \rho_k^0)^2 \\ & + \sum_{i=1}^{N^p} w_i (u_i^{(3)}(\mathbf{X}) - u_i^{\text{ref}(3)}) - \sum_{j=1}^{N^v} \mathbf{p}_j^T \mathbf{v}_j(\mathbf{X}) \end{aligned} \tag{13}$$

where $u_i^{(3)}(\mathbf{X})$ is the component of $\mathbf{u}_i(\mathbf{X})$ corresponding to the x_3 -direction. Then, an equilibrium state is obtained by solving the following energy minimization problem:

$$\begin{aligned} \min_{\mathbf{X}} \quad & \Pi(\mathbf{X}) \\ \text{s.t.} \quad & \mathbf{C}(\mathbf{X}) = \mathbf{0} \end{aligned} \tag{14}$$

In this study, the *path parameter* is introduced, and the magnitude of the forced displacements and/or the loads are assumed to be the function of the scalar path parameter ξ only. The pair of the path parameter ξ and the solution \mathbf{X} to Problem (14) for a given ξ is referred to as the *equilibrium point*. Problem (14) is solved by the augmented Lagrangian method (ALM) [13]. The augmented Lagrangian $L(\mathbf{X})$ with the penalty parameter γ and the Lagrange multipliers $\boldsymbol{\lambda} \in \mathbb{R}^M$ is defined as

$$L(\mathbf{X}) = \Pi(\mathbf{X}) + \mathbf{C}(\mathbf{X})^T \left(\boldsymbol{\lambda} + \frac{\gamma}{2} \mathbf{C}(\mathbf{X}) \right) \tag{15}$$

The solution to Problem (14) is obtained by repeatedly solving the following optimization problem:

$$\min_{\mathbf{X}} L(\mathbf{X}) \tag{16}$$

with constant $\boldsymbol{\lambda}$ while updating the multiplier as $\boldsymbol{\lambda} \leftarrow \boldsymbol{\lambda} + \gamma \mathbf{C}$ until the maximum absolute value among the components of $\mathbf{C}(\mathbf{X})$ becomes smaller than the user-specified tolerance C_{tol} . γ is automatically updated in the process of the ALM based on Ref. [13]. At an exact equilibrium point (\mathbf{X}, ξ) , $dL/dX_j = 0$ holds for all $j = 1, \dots, N$, and the convergence of Problem (16) is evaluated by comparing the maximum value among $|dL/dX_j|$ ($j = 1, \dots, N$) to the user-specified tolerance E_{tol} .

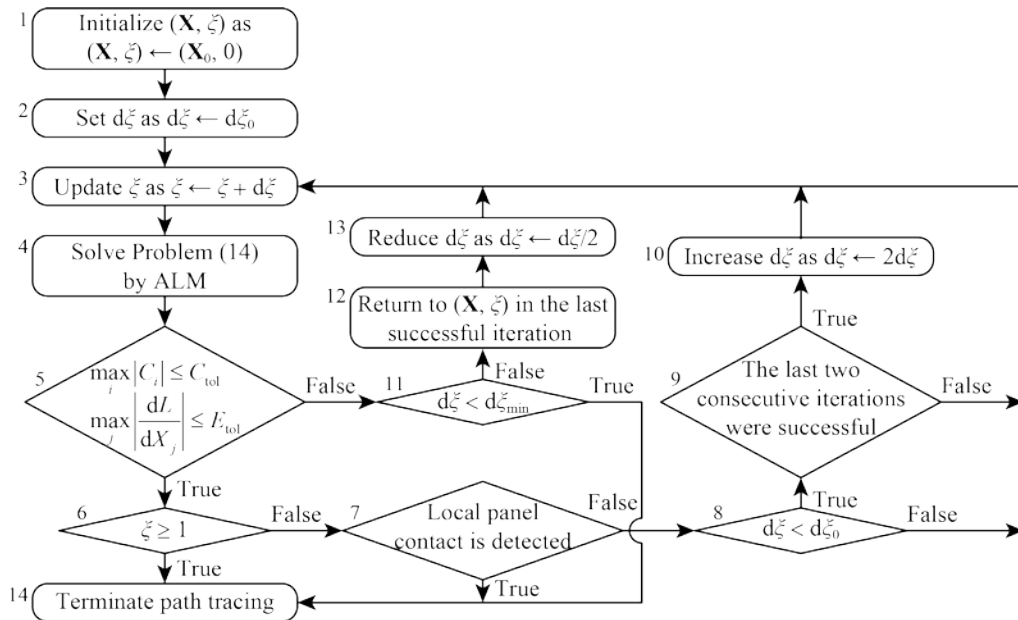


Figure 5: Flowchart of the equilibrium path tracing

4.2. Tracing an Equilibrium Path

An *equilibrium path* is the trajectory of the equilibrium point (\mathbf{X}, ξ) and traced by successively solving Problem (14) by the ALM while updating the path parameter as $\xi \leftarrow \xi + d\xi$ where $d\xi$ is the increment of ξ . In this study, the displacement control method is employed; i.e., each forced displacement $v_j^{d(k)}$ ($\{j, k\} \in \mathcal{J}^d$) is specified at each step of the equilibrium point search as

$$v_j^{d(k)} = \xi \tilde{v}_j^{d(k)} \quad (17)$$

where ξ increases from 0 to 1 at the final step when $v_j^{d(k)}$ reaches the target forced displacement $\tilde{v}_j^{d(k)}$. The point loads \mathbf{p}_j on vertices are assumed to be constant throughout the path tracing.

The procedure of the equilibrium path tracing is summarized in Fig. 5. At the initial step of the analysis (Step 1 in Fig. 5), \mathbf{X} is initialized as $\mathbf{X} = \mathbf{X}_0$ where \mathbf{X}_0 represents the initial imperfection. Problem (14) is solved so that $\max_i |C_i| \leq C_{tot}$ and $\max_j |dL/dX_j| \leq E_{tot}$. However, if these conditions are not satisfied, the step size $d\xi$ is reduced by half (Step 13). The reduced $d\xi$ is restored to $2d\xi$ if the equilibrium points are successfully found in the consecutive iterations (Step 10) to accelerate the analysis. The path tracing terminates when ξ

reaches 1, $d\xi$ decreases less than the specified lower bound $d\xi_{min} > 0$, or the local face contact between the adjacent panels is detected.

5. EXAMPLES

5.1. Settings

The analysis is carried out by using a Python 3.9 program. Problem (16) in Sec. 4 is solved by using BFGS algorithm [14] available in the library `scipy.optimize.minimize` for the equilibrium path tracing. The units of length and force are omitted because they do not influence the analysis results.

Figure 6 shows the crease pattern to be analyzed. All the vertices are on the x_1x_2 -plane in the initial shape. As indicated in green, the displacements of the vertices on the shorter boundaries are fixed, and the forced displacements are assigned along the x_1 -axis as shown by the purple arrows. The orange arrows represent the loads in positive x_2 -direction. The weight per unit area of each panel is 20, and the rotational stiffness per unit length of each crease line is 10. In the equilibrium path tracing, three types of initial imperfections based on sinusoidal functions are assigned to the panel translations in x_3 -direction as shown in Fig. 7. The parameters are set as $C_{tot} = E_{tot} = 10^{-4}$ and $d\xi_{min} = 10^{-5}$ for all the following trials.

For an intuitive understanding of the path tracing results, a physical model has also been constructed

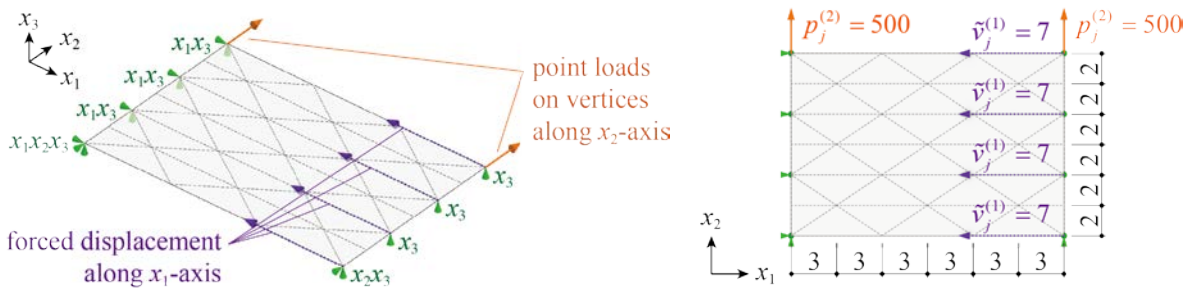


Figure 6: Initial flat shape, panel dimension, and boundary conditions

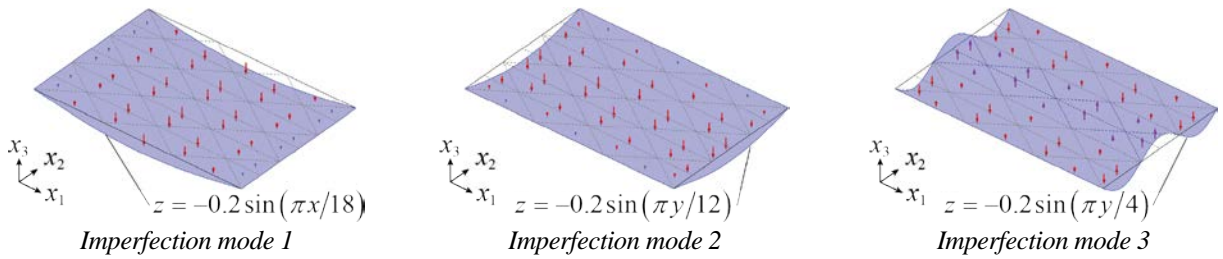


Figure 7: Initial imperfection of face displacements in z -direction based on a sinusoidal function

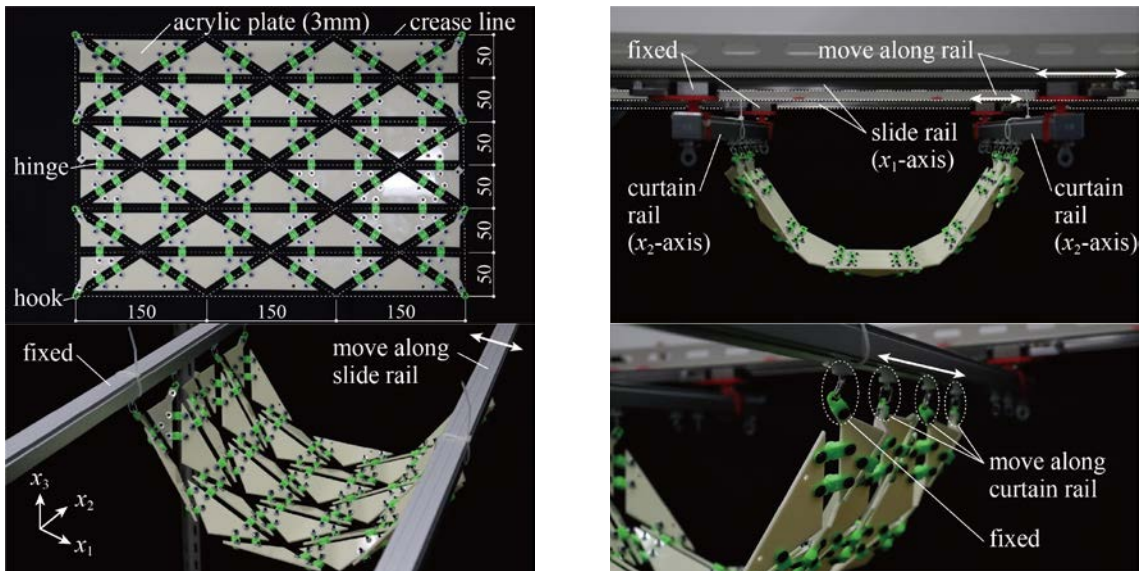


Figure 8: Experimental model

as shown in Fig. 8. The model is hanged from the curtain rails at the hooks attached at the vertices, and the hooks in front are fixed to the rails. The curtain rail on the right side of the picture can move along the slide rails while remaining parallel to the left rail. As we focus on checking the deformation modes and the locking phenomenon of the crease lines, the point loads are not introduced in this model. However, friction provides resistance to the displacements in the direction along the curtain rails.

5.2. Infinitesimal Mechanism Analysis

The infinitesimal mechanism analysis introduced in Sec. 3 is carried out for the initial flat state. The size of compatibility matrix $d\bar{C}/d\mathbf{X}$ is 341×252 , and its

rank is 229. Therefore, the number of kinematic and statical indeterminacies are 23 and 112, respectively. The orthonormal infinitesimal mechanism modes $\bar{\mathbf{X}}'_1, \dots, \bar{\mathbf{X}}'_{23} \in \mathbb{R}^{252}$ cannot be uniquely determined only from Eq. (9), and we determine them as shown in Fig. 9 so that the following matrix is diagonalized and its diagonal elements are arranged in ascending order to reflect the bending stiffness of the model:

$$\begin{bmatrix} \bar{\mathbf{X}}_1^{\prime T} \\ \vdots \\ \bar{\mathbf{X}}_{23}^{\prime T} \end{bmatrix} \begin{bmatrix} \frac{d\rho_1}{dX_1} & \dots & \frac{d\rho_{54}}{dX_1} \\ \vdots & \ddots & \vdots \\ \frac{d\rho_1}{dX_{252}} & \dots & \frac{d\rho_{54}}{dX_{252}} \end{bmatrix} \begin{bmatrix} K_1 & 0 \\ \vdots & \vdots \\ 0 & K_{54} \end{bmatrix} \begin{bmatrix} \frac{d\rho_1}{dX_1} & \dots & \frac{d\rho_1}{dX_{252}} \\ \vdots & \ddots & \vdots \\ \frac{d\rho_{54}}{dX_1} & \dots & \frac{d\rho_{54}}{dX_{252}} \end{bmatrix} \begin{bmatrix} \bar{\mathbf{X}}'_1 & \dots & \bar{\mathbf{X}}'_{23} \end{bmatrix}$$

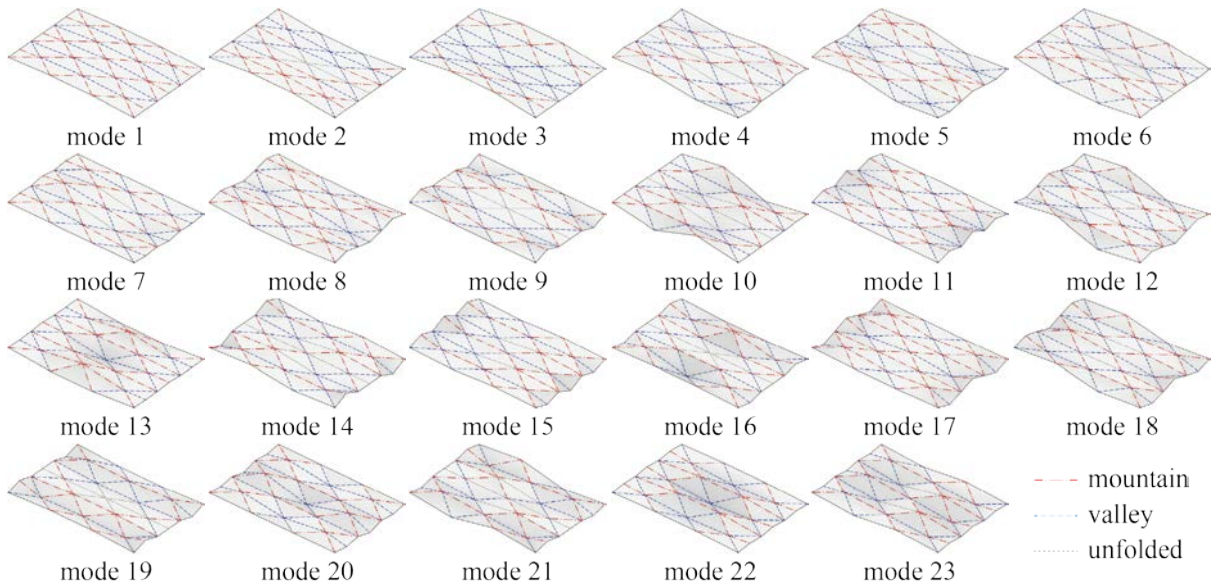


Figure 9: Orthonormal infinitesimal mechanism modes

Table 1: Deformed shapes around $\xi = 0.2$ or the final step of path tracing with different step sizes

	Without initial imperfection			Imperfection mode 2		
	$d\xi_0 = 0.005$	$d\xi_0 = 0.010$	$d\xi_0 = 0.015$	$d\xi_0 = 0.005$	$d\xi_0 = 0.010$	$d\xi_0 = 0.015$
$d\xi_{ini} = 0.005$						
$d\xi_{ini} = 0.010$						
$d\xi_{ini} = 0.015$						
$d\xi_{ini} = 0.020$						

Then, in the first-order infinitesimal mechanism, the stiffness of the model is lowest in the direction of $\bar{\mathbf{X}}'_1$. Any first-order infinitesimal mechanism $\mathbf{X}' \in \mathbb{R}^{252}$ can be represented by a linear combination of $\bar{\mathbf{X}}'_1, \dots, \bar{\mathbf{X}}'_{23}$ with the arbitrary real coefficients a_1, \dots, a_{23} as

$$\mathbf{X}' = a_1 \bar{\mathbf{X}}'_1 + \dots + a_{23} \bar{\mathbf{X}}'_{23}$$

Note that the vertices move almost only along the x_3 -axis in the first-order infinitesimal mechanism. Eq (12) for the existence of the second-order infinitesimal mechanism turns into 19 independent

quadratic equations for a_1, \dots, a_{23} . These quadratic equations qualify the combination of a_1, \dots, a_{23} to make \mathbf{X}' the potential finite mechanism. This limitation of the combination of the coefficients may lead to the bifurcation behavior of the equilibrium path investigated in the following subsections.

5.3. Instability and Bifurcation at the Flat State

This section demonstrates that the equilibrium path obtained by the method proposed in Sec. 4 is highly influenced by the size of the initial path parameter increment as well as the initial imperfection. As summarized in Table 1, we have carried out the path

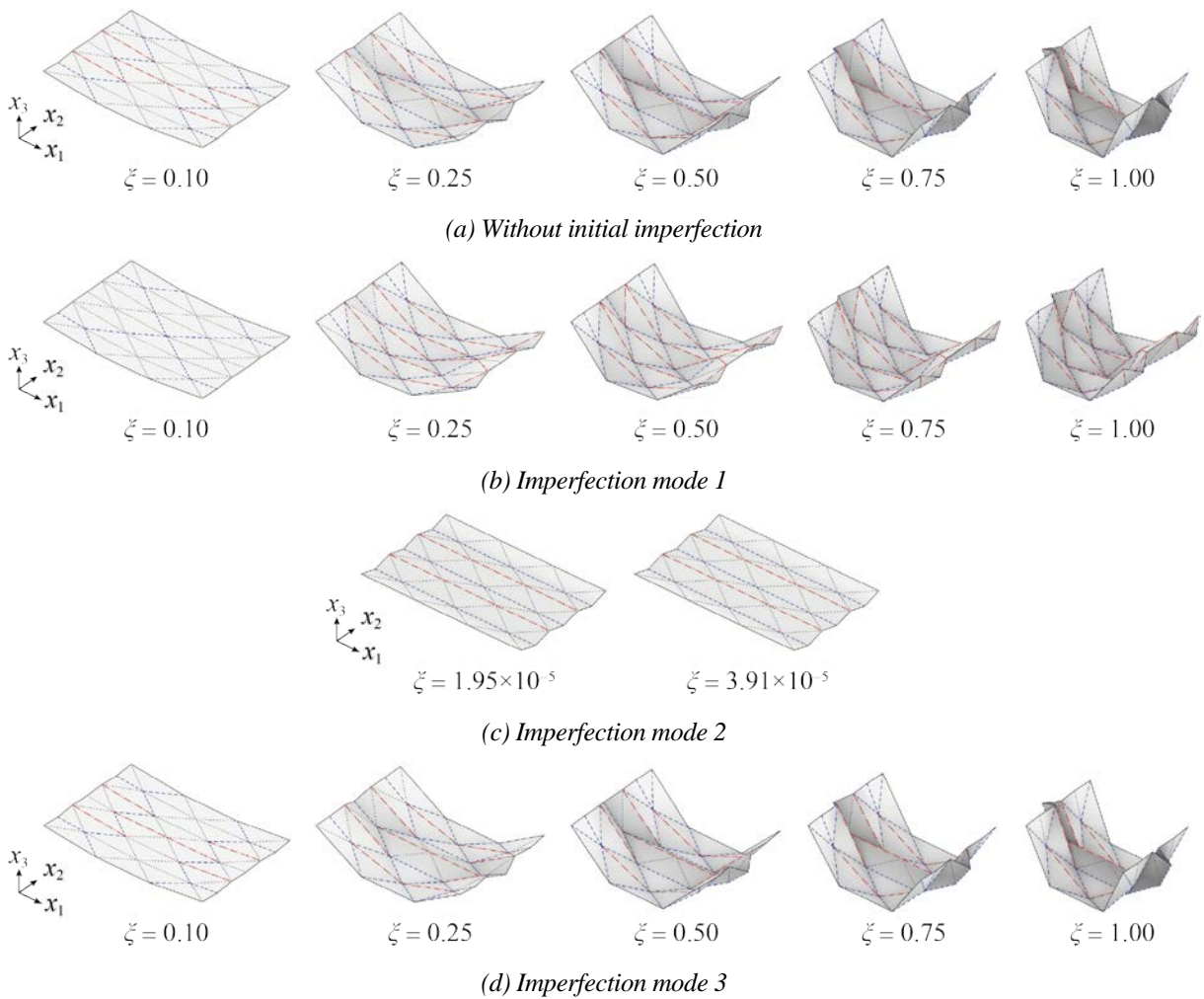


Figure 10: Deformation paths

tracing without initial imperfection and with the imperfection mode 2 shown in Fig. 7 by changing the standard step size as $d\xi_0 = 0.005, 0.010,$ or 0.015 in the path tracing procedure except for the first equilibrium point search step. To investigate the influence of the initial step size, the different step size $d\xi_{ini} = 0.005, 0.010, 0.015,$ or 0.020 are used to find the first equilibrium points. Since the deformation mode (assignment of the mountain and valley to the crease lines) hardly changes after $\xi = 0.2$, we show the deformed shape at the step around $\xi = 0.2$ or the final step, if the analysis terminate before $\xi = 0.2$, in Table 1 to better illustrate the deformation. As shown in Table 1, different equilibrium paths are obtained by changing the initial step size $d\xi_{ini}$, while the standard step size $d\xi_0$ for the second and later equilibrium point search does not significantly change the equilibrium paths.

5.4. Path Tracing with Initial Imperfection

In this section, we will show the result of the equilibrium path tracing from the perfectly flat state and the results with the initial imperfections shown in Fig. 7. The deformation modes and the locking phenomenon of the crease lines are also investigated by the physical experimental model shown in Fig. 8.

Figure 10 shows the deformation path with $d\xi_0 = 0.05$. The paths shown in Fig. 10(a) and (d) are approximately the same. By assigning the different initial imperfection, the different paths can be obtained. The deformed shape may contain the unfolded crease lines, and these crease lines may be locked; e.g., in the equilibrium path shown in Fig. 10(c) where the path tracing has been terminated with small ξ , the diagonal crease lines are locked under the forced displacements in the x_1 -direction, and the forced displacements cannot increase due to the locked mechanism.

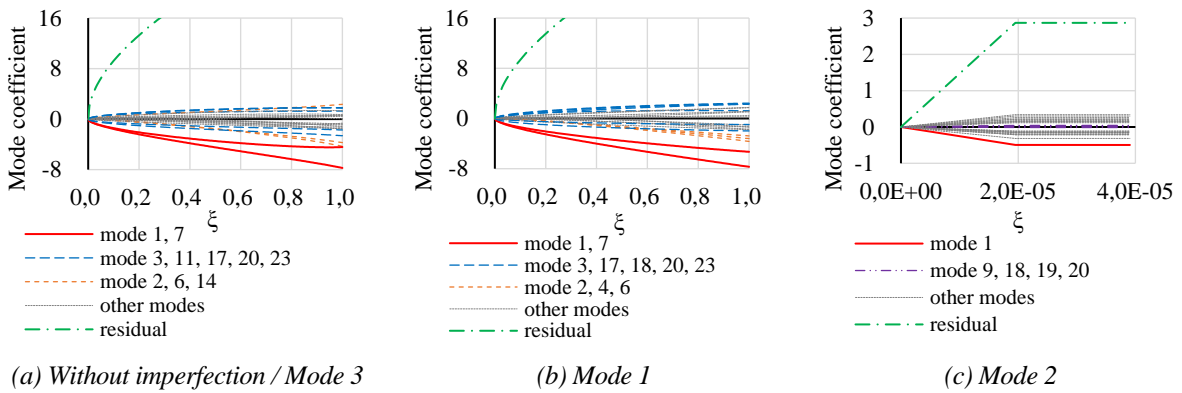


Figure 11: Value of coefficients of infinitesimal mechanism modes and the norm of residual vector

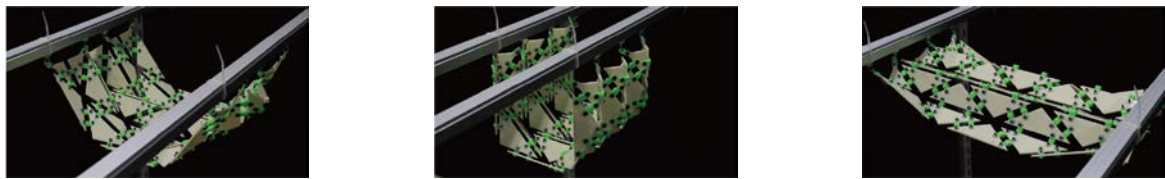


Figure 12: Approximate reproduction of analysis results in Fig. 6 by experimental models

At every equilibrium point on the paths obtained without initial imperfection and with the imperfection modes 1 and 3, the rank of compatibility matrix is 248, and the number of kinematic indeterminacy is 4, while those are 247 and 5, respectively, at every equilibrium point on the path with imperfection mode 2. The values of coefficients of the first-order infinitesimal mechanism modes investigated in Sec. 5.2 at an equilibrium point \mathbf{X} are computed by $a_i = \langle \mathbf{X}, \bar{\mathbf{X}}_i' \rangle$ ($i=1, \dots, 23$), and the norm of the residual is computed as $\left\| \mathbf{X} - \sum_{i=1}^{23} a_i \bar{\mathbf{X}}_i' \right\|$. These values are plotted in Fig. 11. It can be seen that the coefficients of mode 1 is significantly larger than those of other modes in every path in Fig. 10, that is reasonable since the bending stiffness of the model is smallest in the direction of mode 1. In addition, since the infinitesimal mechanism modes do not include the vertex displacements in x_1 - and x_2 - directions, the norm of residual is quite large on every paths, which corresponds to the higher-order term.

The locking phenomenon of the crease lines is also confirmed by the physical experimental model as shown in Fig. 12, which approximately reproduces each deformation mode in Fig. 10. In the experimental model, the curtain rail on the right side of the picture cannot move to the negative x_1 -direction due to the locked hinges.

6. CONCLUSIONS

This paper has presented the panel-pin model, which has been applied to the infinitesimal mechanism analysis and the geometrically nonlinear equilibrium path analysis of the rigid origami with multiple degrees of freedom of mechanism. It has been shown that the multiple equilibrium paths can be obtained by assigning different initial imperfection in the investigated crease pattern.

ACKNOWLEDGEMENTS

This work is supported by JSPS KAKENHI Grant Numbers JP20J21650, JP19K04714 and JST CREST Grant Number JPMJCR1911.

DATA AVAILABILITY

Some or all of the derived data supporting the findings of this study are available from the corresponding author on reasonable request.

REFERENCES

[1] S. A. Zirbel, R. J. Lang, M. W. Thomson, D. A. Sigel, P. E. Walkemeyer, B. P. Trease, and S. P. Magleby, L. L. Howell, "Accommodating thickness in origami-based deployable arrays," *J. Mech. Design*, vol. 135, no. 11, paper no. 111005, Oct. 2013. (DOI: [10.1115/1.4025372](https://doi.org/10.1115/1.4025372))

[2] C. H. Belke, and J. Paik, "Mori: A Modular Origami Robot," *IEEE/ASME Trans.*

- Mechatron.*, vol. 22, no. 5, pp. 2153-2164, Oct. 2017. (DOI: [10.1109/TMECH.2017.2697310](https://doi.org/10.1109/TMECH.2017.2697310))
- [3] P. M. Reis, F. L. Jiménez, and J. Marthelot, "Transforming architectures inspired by origami," *Proc. Natl. Acad. Sci. U.S.A.*, vol. 112, no. 40, pp. 12234-12235, Oct. 2015. (DOI: [10.1073/pnas.1516974112](https://doi.org/10.1073/pnas.1516974112))
- [4] Y. Zhu, M. Schenk, and E. T. Filipov, "A review on origami simulations: from kinematics, to mechanics, toward multiphysics," *Appl. Mech. Rev.*, vol. 74, no. 3, paper no. 030801, Aug. 2022. (DOI: [10.1115/1.4055031](https://doi.org/10.1115/1.4055031))
- [5] T. Tachi, "Simulation of rigid origami," in *Proc. 4th international meeting of origami science, mathematics, and education (Origami4)*, R. J. Lang, Ed. Natick: AK Peters, 2009, pp. 175-187.
- [6] Z. He and S. D. Guest, "On rigid origami III: Local rigidity analysis," *Proc. Math. Phys. Eng. Sci.*, vol. 478, issue 2258, paper no. 20210589, Feb. 2022. (DOI: [10.1098/rspa.2021.0589](https://doi.org/10.1098/rspa.2021.0589))
- [7] M. Schenk and S. D. Guest, "Origami folding: A structural engineering approach," in *Proc. 5th international meeting of origami science, mathematics, and education (Origami5)*, P. Wang-Iverson, R. J. Lang, and M. Yim, Eds. Boca Raton: CRC Press, 2011, pp. 291-303.
- [8] T. Zhang, K. Kawaguchi and M. Wu, "A folding analysis method for origami based on the frame with kinematic indeterminacy," *Int. J. Mech. Sci.*, vol. 146-147, pp. 234-248, Oct. 2018. (DOI: [10.1016/j.ijmecsci.2018.07.036](https://doi.org/10.1016/j.ijmecsci.2018.07.036))
- [9] K. Hayakawa and M. Ohsaki, "Form generation of rigid origami for approximation of a curved surface based on mechanical property of partially rigid frames," *Int. J. Solids Struct.*, vol. 216, pp. 182-199, May 2021. (DOI: [10.1016/j.ijsolstr.2020.12.007](https://doi.org/10.1016/j.ijsolstr.2020.12.007))
- [10] K. Hayakawa and M. Ohsaki, "Equilibrium path and stability analysis of rigid origami using energy minimization of frame model," *Front. Built Environ.*, vol. 8, Aug. 2022. (DOI: [10.3389/fbuil.2022.995710](https://doi.org/10.3389/fbuil.2022.995710))
- [11] M. Géradin and A. Cardona, *Flexible Multibody Dynamics: A Finite Element Approach*, London: Wiley, 2007
- [12] R. Watada and M. Ohsaki, "Series expansion method for determination of order of 3-dimensional bar-joint mechanism with arbitrarily inclined hinges," *Int. J. Solids Struct.*, vol. 141-142, pp. 78-85, June 2018. (DOI: [10.1016/j.ijsolstr.2018.02.012](https://doi.org/10.1016/j.ijsolstr.2018.02.012))
- [13] E. G. Birgin and J. M. Martínez, "Augmented Lagrangian method with nonmonotone penalty parameters for constrained optimization," *Comput. Optim. Appl.*, vol. 51, pp. 941-965, Feb. 2012. (DOI: [10.1007/s10589-011-9396-0](https://doi.org/10.1007/s10589-011-9396-0))
- [14] J. Nocedal and S. J. Wright, *Numerical Optimization*, New York: Springer, 2006.